

A Weak Temperature Gradient Framework to Quantify the Causes of Potential Intensity Variability in the Tropics

RAPHAËL ROUSSEAU-RIZZI^a AND KERRY EMANUEL^a

^a *Lorenz Center, Department of Earth, Atmospheric and Planetary Sciences, Massachusetts Institute of Technology, Cambridge, Massachusetts*

(Manuscript received 15 February 2021, in final form 9 August 2021)

ABSTRACT: Potential intensity (PI) has been shown to have a linear sensitivity to sea surface temperature (SST) of about $8 \text{ m s}^{-1} \text{ K}^{-1}$, which is close to the sensitivity of PI in simulations subject to a weak temperature gradient (WTG) approximation. This suggests that most of the PI variance is associated with local rather than global SST variations. We verify that PI perturbations are approximately linear in SST, with slopes of $1.8 \pm 0.2 \text{ m s}^{-1} \text{ K}^{-1}$ in radiative–convective equilibrium (RCE) and $9.1 \pm 0.9 \text{ m s}^{-1} \text{ K}^{-1}$ in WTG. To do so, we simulate the sensitivity of both RCE and WTG states in a single-column model (SCM) perturbed by changing in turn CO_2 concentration, aerosol concentrations, prescribed SST, and surface winds speeds. While PI is much more sensitive to SST in WTG than in RCE simulations, the SST itself is much less sensitive to radiative forcing in WTG than in RCE because of the absence of strong atmospheric response. Using these results, we develop a linear model, based on SST and midlevel saturation MSE perturbations, to partition SST and PI perturbations between local components occurring under a WTG constraint and global components that are representative of an RCE state. This model explains up to 95% of the variability of PI in reanalysis. The SCM-derived linear model coefficients are statistically indistinguishable from coefficients from a linear fit of reanalysis PI to SST and midlevel saturation MSE in most ocean basins. Our model shows that North Atlantic PI variations are explained almost entirely by local forcings in recent decades.

KEYWORDS: Atmosphere; Tropical cyclones; Climate variability

1. Introduction

Potential intensity (PI; Emanuel 1986, 1988; Bister and Emanuel 1998; Bryan and Rotunno 2009) is a theoretical bound on the maximum achievable wind speed in tropical cyclones (TCs). PI has been shown to provide fairly accurate bounds on the maximum wind speed in TCs both in observations (Emanuel 2000) and in models (Rousseau-Rizzi and Emanuel 2019) and can be seen as an indication of how favorable the thermodynamic environment is to the maintenance of strong TCs. It is one of the main predictors of TC activity as represented by the power dissipation index (PDI; Emanuel 2007), an indication of the total amount of energy dissipated by all TCs over a given basin and a given TC season. In other words, PI is an important predictor of the amount of power dissipated by TCs and thus, of their destructive potential. For that reason, understanding the causes of past PI variability is useful to help predict future variability in TC activity.

TC intensity variability is often attributed to sea surface temperature (SST) variability, and Vecchi and Soden (2007) showed that PI correlates well with SST spatial anomalies and that the slope of the linear regression is near $8 \text{ m s}^{-1} \text{ K}^{-1}$. PI can be expressed as

$$\text{PI}^2 = \frac{C_k}{C_D} \frac{T_s - T_o}{T_o} (h_s^* - h_m^*), \quad (1)$$

(Bister and Emanuel 1998; Wing et al. 2015) where C_k and C_D are the surface exchange coefficients of enthalpy and momentum, T_s is the sea surface temperature, T_o is the outflow

temperature of the storm, h_s^* is the saturation moist static energy (MSE) at sea surface temperature, and h_m^* is the tropospheric saturation MSE. Here we have made use of the fact that, within the assumption of quasi equilibrium (Arakawa and Schubert 1974) with a coupled boundary layer, $h_b = h_m^*$, where h_b is the boundary layer MSE.

PI and SST changes result from global (e.g., Sobel et al. 2019) or from local (e.g., Mann and Emanuel 2006) forcing. Global forcing is generally understood as influencing the whole tropical region as if it were, on average, in a state of radiative–convective equilibrium (RCE). In RCE, a positive forcing causes an increase in sea surface temperature and h_s^* , which tends to increase PI, and an increase in h_m^* , which mitigates the increase in PI. However, the tropical atmosphere has large Rossby radii of deformation, especially at low latitudes. According to the weak temperature gradient approximation (WTG; Sobel and Bretherton 2000), this means that h_m^* is almost horizontally uniform and can only change globally, not regionally. The implication is that a local forcing that increases SST also increases h_s^* but does not increase h_m^* since the additional energy supplied to the atmosphere is exported in the form of gravity waves. In the absence of a change in h_m^* , PI is much more sensitive to SST changes in a column constrained by WTG than to changes in RCE (Ramsay and Sobel 2011; Emanuel and Sobel 2013). Ramsay and Sobel (2011) show that the sensitivity of PI to SST in an RCE system with imposed SST is around $1 \text{ m s}^{-1} \text{ K}^{-1}$, whereas in a WTG-constrained column it is near $8 \text{ m s}^{-1} \text{ K}^{-1}$, which is much larger. The PI–SST regression coefficient found by Vecchi and Soden (2007) in reanalysis datasets is also close to $8 \text{ m s}^{-1} \text{ K}^{-1}$, which suggests that local forcings and their effects on SST dominate PI variability worldwide.

Corresponding author: Raphaël Rousseau-Rizzi, rrizzi@mit.edu

DOI: 10.1175/JCLI-D-21-0139.1

© 2021 American Meteorological Society. For information regarding reuse of this content and general copyright information, consult the AMS Copyright Policy (www.ametsoc.org/PUBSReuseLicenses).

For this reason there is particular interest in understanding the forcings responsible for local SST variability. Here, we will be focusing on SST as a proxy for PI variability because SST variability is well measured and studied. In the tropical North Atlantic (TNA), SST multidecadal variability and the concurrent effects on PI have been attributed to a variety of causes such as the Atlantic multidecadal oscillation (AMO; Zhang and Delworth 2006), sulfate aerosol forcing (Mann and Emanuel 2006; Booth et al. 2012; Dunstone et al. 2013), Saharan dust forcing (Strong et al. 2015, 2018), and surface wind and cloud feedbacks (e.g., Evan et al. 2011, 2016). Some of these explanations such as dust and cloud feedbacks are complementary and some, like the AMO and anthropogenic aerosols, are competing. Hence there exist multiple possible mechanisms that can act to set the SST in the TNA and that could help explain hurricane activity variability. Notably, the “hurricane drought” (decreased hurricane activity) of the 1970s and 1980s has resisted a single explanation (e.g., Villarini and Vecchi 2013). In this paper, we attempt to introduce a linear framework that can be used to compare and contrast these influences on SST and PI, using a well-known strong constraint on tropical thermodynamics, WTG.

Objectives

In this paper, we aim to

- 1) show that PI perturbations are approximately linear in SST, with different slopes in WTG and RCE;
- 2) show that SST perturbations can be partitioned between local and global components, which allows one to partition PI variations as well; and
- 3) evaluate the local and global contributions to PI variability in the North Atlantic MDR and in other basins.

First, section 2 discusses the theoretical sensitivity of PI to SST in RCE and WTG, then section 3 describes the SCM setup and the data and reanalyses used in the study and section 4 describes and explains the results of the sensitivity experiments. Next, section 5 introduces the linear model for PI and obtains its coefficients, and section 6 applies the model to reanalysis products. Finally, section 7 discusses the results and section 8 summarizes and concludes.

2. Analytical estimates

Analytical estimates for PI sensitivity can be obtained fairly easily for WTG-constrained columns. In such a system, the free troposphere is constrained to a constant value of h^* , a thermodynamic variable, but it is not an energetically closed system. In RCE, the main constraint in the free troposphere is that of energy balance, which is much more complex as it relates to equilibrium climate sensitivity (ECS). For that reason, it is easiest to approach PI sensitivity in WTG from thermodynamic forms of the PI equation, and PI sensitivity in RCE from energy balance forms of the PI equation (e.g., Emanuel 2007).

a. WTG PI sensitivity

We start by taking the derivative of the log of PI Eq. (1) with respect to T_s , along with the assumption that the outflow

temperature is independent of the sea surface temperature ($dT_o/dT_s = 0$). In practice, outflow temperatures can vary up to 10°C degrees on a seasonal time scale (Gilford et al. 2017) and could influence long-term PI trends. However, statistically significant influences on PI have not yet been found in reanalysis data (Wing et al. 2015). We write

$$\frac{2}{\text{PI}} \frac{d\text{PI}}{dT_s} = \frac{1}{T_s - T_o} + \frac{1}{(h_s^* - h_m^*)} \left(\frac{dh_s^*}{dT_s} - \frac{dh_m^*}{dT_s} \right), \quad (2)$$

where subscript s denotes the surface and m denotes any point in the free troposphere. In the dilute limit, when the water vapor mixing ratio is much smaller than one, we can write saturation MSE as

$$h^* = c_{pd}T + L_v r^* + \Phi, \quad (3)$$

where c_{pd} is the heat capacity of dry air at constant pressure, L_v is the latent heat of evaporation, r^* is the water vapor saturation mixing ratio, and Φ is the geopotential. Since r^* is a function of T and dry-air pressure p_d , h^* is a function of T , p_d , and Φ , and we have

$$\frac{dh^*}{dT_s} = \frac{\partial h^*}{\partial T} \frac{dT}{dT_s} + \frac{\partial h^*}{\partial p_d} \frac{dp_d}{dT_s} + \frac{\partial h^*}{\partial \Phi} \frac{d\Phi}{dT_s}. \quad (4)$$

Neglecting the sensitivity of latent heat to temperature and using the equation of Clausius–Clapeyron, we have, within a few percent,

$$\frac{\partial h^*}{\partial T} \approx c_{pd} + \frac{L_v^2 r^*}{R_v T^2}, \quad (5)$$

where R_v is the ideal gas constant for water vapor. At the surface, $dT_s/dT_s = 1$, and the geopotential is constant. We also neglect the contribution of surface p_d changes to saturation MSE changes so that

$$\frac{\partial h^*}{\partial p_d} \frac{dp_d}{dT_s} \approx 0. \quad (6)$$

In addition, if we neglect virtual effects, the WTG approximation implies that h_m^* does not change in response to local SST changes. Hence, we can write

$$\left. \frac{dh_s^*}{dT_s} \approx \frac{\partial h^*}{\partial T} \right|_s, \quad \frac{dh_m^*}{dT_s} \approx 0, \quad (7)$$

and finally

$$\frac{d\text{PI}}{dT_s} \approx \frac{\text{PI}}{2} \left[\frac{1}{T_s - T_o} + \frac{1}{(h_s^* - h_m^*)} \left(c_{pd} + \frac{L_v^2 r^*}{R_v T_s^2} \right) \right]. \quad (8)$$

This allows one to estimate the sensitivity of PI to SST in a column in quasi equilibrium (QE) and under a WTG constraint. Typical values such as $T_o = 200$ K, $T_s = 303$ K, and $\text{PI} = 75 \text{ m s}^{-1}$ yield $r^* = 27 \text{ g kg}^{-1}$, $h_s^* = 3.75 \times 10^5 \text{ J kg}^{-1}$, $h_m^* = 3.56 \times 10^5 \text{ J kg}^{-1}$, and a sensitivity of about $10.1 \text{ m s}^{-1} \text{ K}^{-1}$, which is somewhat higher than reported in the literature. Since the derivation

relies only on QE and WTG assumptions, and the result depends only on thermodynamic variables, a departure between the PI sensitivity estimated from the thermodynamic state using Eq. (8) and observed or modeled sensitivity must arise from a violation of either QE or WTG assumptions. For example, an environmental profile set by an entraining parcel could result in a smaller-than-theoretical sensitivity. Next, we consider the RCE problem, which is a bit more complicated.

b. RCE PI sensitivity

In RCE, PI sensitivity will again be assessed starting from Eq. (2), but this time, contrarily to the WTG case, $dh_m^*/dT_s \neq 0$, so that the sensitivity of PI cannot be deduced simply from thermodynamics. In RCE, and under the assumption of boundary layer quasi equilibrium, the value of dh_m^*/dT_s arises from the radiative properties of the atmosphere and the surface, so the sensitivity of PI relates to the climate sensitivity of the tropics. Hence, no simple analytical solution is available and progress can only be made by writing the surface thermodynamic disequilibrium in terms of the energy balance at the surface. Following Emanuel (2007), we write

$$F_s + Q_{oc} = \rho_d C_k |V_s| (h_s^* - h_m^*), \quad (9)$$

where F_s is the net radiative flux at the surface, Q_{oc} is the vertically integrated ocean heat flux convergence, and $|V_s|$ is the magnitude of the environmental surface wind speed. The RHS of the equation is a bulk formulation for the latent and sensible heat fluxes from the surface in equilibrium. In a climate change scenario, the response of all of the terms in this equation needs to be considered, as a change in global radiative forcing might affect the surface wind speed and the ocean heat flux convergence as well as the net surface radiative flux. In equilibrium, we can write

$$F_{atm} + Q_{atm} = F_s + Q_{oc}, \quad (10)$$

where F_{atm} is the net radiative heat flux integrated over the whole atmosphere and Q_{atm} is the net dynamical heat flux convergence integrated over the atmosphere. Any study attempting to assess the full impact of a global forcing on PI would need to take into account changes in the large-scale circulation. Here, we focus on the narrower topic of single column RCE where the wind speed is imposed and there is no atmospheric heat export. Then, when SST is determined by energy balance, $Q_{oc} = 0$, and when SST is imposed, Q_{oc} is implied. Equivalently, one could specify Q_{oc} to a nonzero value and compute SST, again by energy balance. In single-column RCE, with $Q_{oc} = 0$, we can think about the sensitivity of net surface radiative flux in terms of net atmospheric cooling, which is a function of the atmosphere radiative properties. Hence, if we substitute Eqs. (9) and (10) into Eq. (2) and we neglect changes in near-surface density, we have

$$\frac{2}{PI} \frac{dPI}{dT_s} = \frac{1}{T_s - T_o} + \frac{1}{F_{atm}} \frac{dF_{atm}}{dT_s} - \frac{1}{|V_s|} \frac{|V_s|}{dT_s}. \quad (11)$$

Neglecting wind speed changes for now, we see that the temperature sensitivity of the turbulent enthalpy (or MSE)

flux, at the surface is equal to that of the net column-integrated radiative cooling of the atmosphere, F_{atm} . Obtaining an analytical estimate for dF_{atm}/dT_s is beyond the scope of this paper but, using a combination of theory and modeling and accounting for water vapor changes only (no CO_2 changes), Jeevanjee and Romps (2018) show that, in RCE,

$$\frac{1}{F_{atm}} \frac{dF_{atm}}{dT_s} \approx 3\% K^{-1}. \quad (12)$$

If we then take surface wind speed, exchange coefficients, and density to be fixed and we substitute this in the formula for PI along with $T_o = 200$ K, $T_s = 303$ K, and $PI = 75$ m s⁻¹, we get

$$\frac{dPI}{dT_s} \approx 1.5 \text{ m s}^{-1} K^{-1}, \quad (13)$$

which is very close to the simulation estimate of Ramsay and Sobel (2011). Interestingly, 1/4 of the total PI sensitivity comes from that of the thermodynamic efficiency. This indicates that, in the global atmosphere, hypothetical changes of outflow temperature of the same order of magnitude as changes in surface temperature could strongly enhance or mitigate the PI sensitivity.

Now if the wind speeds are allowed to vary and we take the mean wind to be 5 m s⁻¹, and the associated sensitivity of SST to wind speed to be approximately -1 K s m⁻¹ [based on Emanuel and Sobel (2013)], we get a contribution to PI sensitivity of approximately 10% K⁻¹, or 7.5 m s⁻¹ K⁻¹, due to wind speed changes alone. This sensitivity is much larger than that due to surface temperature changes at fixed wind speeds because the fractional variation of wind speed is much larger than that of net surface radiative heating, for a given temperature change. This sensitivity is similar to that of PI under a WTG constraint, which we will discuss in section 4. Since tropical SST changes on the large scale are attributed mostly to changes in radiative forcing, and not to large-scale changes in wind speed, we can expect the observed large-scale PI sensitivity to be closer to 1.5 than to 7.5 m s⁻¹ K⁻¹.

3. Methodology

Next we obtain the sensitivity of PI to SST in simulations. We use the Massachusetts Institute of Technology (MIT) single-column model (Bony and Emanuel 2001), which uses the convection parameterization of Emanuel and Živković-Rothman (1999) and the radiation parameterizations of Fouquart et al. (1980) and Morcrette (1991). The simulations use vertical profiles of cloud fraction that are fixed in pressure because allowing the cloud fraction to evolve adds a lot of noise to the sensitivity experiment results. That choice means that the altitude of the cloud profile increases slightly when the air column warms. Water vapor and its effects on radiation are allowed to evolve. The ocean is a 2-m-deep slab ocean, to allow for sea surface temperature to vary and to maintain energy balance in RCE, except for the prescribed SST simulations. The small depth of the ocean allows the system to reach equilibrium faster. In this study we are not concerned with the time scales of the evolution toward equilibrium, hence this choice does not affect the results.

We run four series of experiments in RCE and three series under a WTG constraint. To enforce the WTG constraint, a large-scale vertical velocity profile is computed at each time step above 850 hPa, such that the associated temperature and moisture tendencies maintain the initial virtual temperature profile exactly. Under the 850-hPa level, the virtual temperature is allowed to evolve freely. We test the sensitivity of the RCE state to CO₂ concentration, and we test both the sensitivity of RCE columns and of WTG-constrained columns to dust aerosol direct effect, to prescribed SST variations, and to near-surface wind variations. CO₂ is varied from 200 to 800 ppm, dust aerosol optical depth (AOD) is varied from 0 to 1, imposed SST is varied from 28.6 to 32.6 K, and surface wind speed is varied from 3 to 14 m s⁻¹. The effect of imposing SST can be likened to imposing some value of column-integrated ocean heat flux convergence. The variety of sensitivity experiments aims to confirm that the choice of dynamical constraint (either RCE or WTG) has a more important influence on the PI–SST relation than does the precise cause of the system perturbation. These experiments are very similar to those of Emanuel and Sobel (2013), who perturbed CO₂, SST, surface winds, and the solar constant in RCE and WTG simulations. The main difference between our choice of experiments and theirs is that where they modified the solar constant, we perturbed dust aerosol concentrations. Since dust is a fairly absorptive aerosol, it acts to heat the atmosphere as it cools the surface.

All simulations are perturbed with respect to a control case which we try to choose as representative of the mean state over the TNA main development region (MDR) during the August–October hurricane season (ASO). In RCE sensitivity experiments, the chosen control case broadly defines the center of the parameter space to be explored and all simulations are independent from one another. In the WTG-constrained column however, the control case also determines the virtual temperature profile above the 850-hPa level based upon which the WTG vertical velocities will be computed. In reanalysis (NOAA 20CR), the mean near-surface wind speed during ASO in the MDR is 4.8 m s⁻¹, so we take our control case to have a near-surface wind speed of 5 m s⁻¹. We will use a dust optical thickness of 0.3 as the ASO MDR-averaged baseline based on Evan and Mukhopadhyay (2010). The control case has 360 ppm CO₂, which is representative of the near past.

In our simulations and in reanalysis data, PI is computed using a nonlinear iterative algorithm developed by Bister and Emanuel (2002), which takes as an input sea surface temperature and vertical profiles of pressure, temperature, and mixing ratio. The algorithm is used instead of Eq. (1) because it accounts for cases where the atmosphere is stable to boundary layer parcels [which Eq. (1) does not] and also accounts for the pressure feedback within the TC. When the atmosphere is not stable, the values and climate sensitivities of PI computed using the algorithm of Bister and Emanuel (2002) are fairly similar to those resulting from Eq. (1). Merlis et al. (2021) found the relative departure of the PI values from both methods to be just a few percent in Earth-like conditions, while the PI sensitivities departed by about 17%. In any case, these differences

should not matter too much for us since the coefficients of the linear model will be determined based on algorithm PI computations and will be compared to data computed similarly. In cases where the boundary layer decouples from the free troposphere, PI can be multivalued. For example, an existing storm translating into such an environment could be sustained and strong (upper PI value), but a new storm could likely not develop (lower PI value) in this environment. This decoupling occurs when the outflow temperature (similar to the level of neutral buoyancy) is very different for a boundary layer parcel and for a parcel saturated at sea surface temperature and eyewall pressure. When computing PI in simulations, we purposely select the lowest of the possible PI values in the few cases where the BL is decoupled because the sensitivity of the high PI value is nonmonotonic across a decoupling of the boundary layer and hence the low PI value is more appropriate to the development of a linear model. A consequence of this choice is that our model will be more appropriate for evaluating PI for the purpose of weak or developing storms when decoupling occurs. Situations where decoupling affects the results will be discussed. In reanalysis data, we use the implementation of the algorithm transcribed for Python by Gilford (2020).

4. Sensitivity experiment results

Figure 1 introduces the results of the sensitivity experiments. Each point in the figure represents either PI or T_s at equilibrium in one simulation, plotted against the corresponding perturbed parameter.

a. CO₂ sensitivity

In the CO₂ panels, we can see PI leveling off as temperature increases. This is partly due to the effect of high CO₂ concentrations where the net infrared flux to the surface stops increasing with temperature which causes the PI profile to flatten even though SST keeps increasing (e.g., O’Gorman and Schneider 2008). In addition, the fixed cloud profile used in the simulations increases stability near the outflow of the TCs, which prevents PI from increasing further. In our simulations, a doubling of CO₂ is associated with an SST change of 1.5–2 K, which is on the low end of the response expected from Earth’s climate.

b. Imposed SST sensitivity

In the next experiment, SST is imposed, which is why the SST plot has a unique slope of 1. The values are the same for both RCE and WTG. The PI–SST relationship conforms reasonably well with the literature, with a slope of about 1.6 m s⁻¹ K⁻¹ in the RCE experiment, and a slope of about 9 m s⁻¹ K⁻¹ in the WTG experiment. The RCE slope is very similar to the 1.4 m s⁻¹ K⁻¹ slope of Ramsay and Sobel (2011) and small modeling differences, such as control simulation background wind, can easily account for the difference. The WTG slope is somewhat higher than the 7.6 m s⁻¹ K⁻¹ introduced by Ramsay and Sobel (2011), which may be due to the fact that in our simulations, the boundary layer decouples from the free troposphere at low temperatures, which

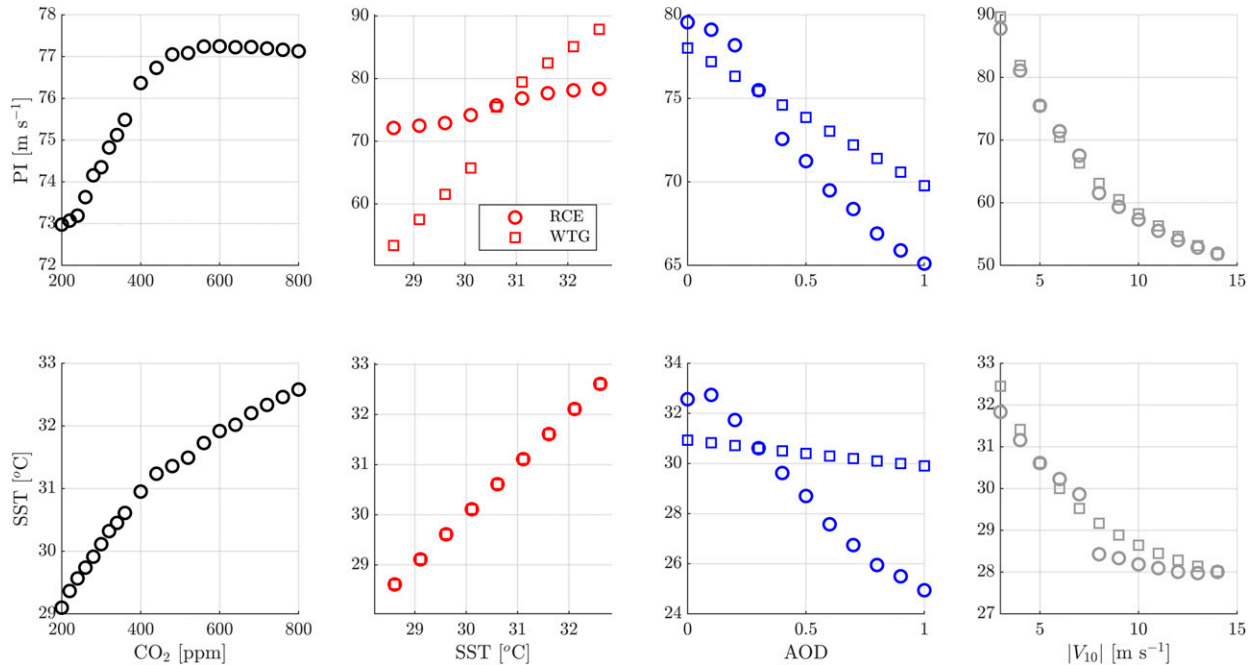


FIG. 1. Sensitivity of (top) PI and (bottom) SST to changes in (left to right) CO_2 concentration (black), aerosol optical depth (blue), imposed SST (red), and near-surface wind speed (gray). All plots superimpose the RCE experiments (circle) to the WTG experiment (squares), except for the CO_2 experiment, which is only performed in RCE.

causes a slightly sharper decrease in PI. These plots do not provide much new insight, but confirm that the simulations are not very different from results from the literature.

c. Aerosol sensitivity

Now looking at the sensitivity of SST to aerosol optical thickness variations, we notice that the slope of SST in WTG is much smaller than that in RCE (-1 K per unit AOD by comparison to -8 K). We surmise that this is due to the atmospheric heat transport by gravity waves implied by the WTG parameterization, which prevents any strong feedback between the atmosphere and the ocean and makes SST less sensitive to aerosol forcing. An interesting consequence of this difference in SST sensitivities to aerosol forcing is that the PI sensitivity to aerosol forcing in RCE is larger than that in WTG, even though the PI–SST slope is much steeper in WTG (as will be seen in Fig. 2). Interestingly, this suggests that the reason why PI variability is dominated by local variability is that the local variability of forcings (like ocean heat flux convergence or aerosol forcing) is much larger than the global variability, and not because PI is intrinsically more sensitive to a given forcing in WTG than in RCE (if anything, it is less sensitive).

d. Wind sensitivity

The wind sensitivity experiments test wind speed variations from 3 to 14 m s^{-1} in unit increments. In contrast to other parameters, which produce very different responses in RCE and in WTG, the results of the wind sensitivity experiments are similar in both cases. Not only are both SST– $|V|$ relations

similar, the PI– $|V|$ relations are as well, and both cases have PI–SST slopes close to $9\text{ m s}^{-1}\text{ K}^{-1}$. One way to understand this similarity is that, in RCE, if we neglect the change in longwave radiation emitted by the surface and assume a constant Bowen ratio, then the atmospheric properties remain identical as surface wind speeds change, and the ocean temperature adjusts to keep the turbulent heat flux constant. This lack of tropospheric temperature change is very similar to what would happen in a WTG scenario, and correspondingly, surface wind perturbations in WTG do not cause large compensating vertical velocities. In other words, under the assumptions mentioned above, both cases are equivalent.

5. Linear PI model

The idea we are pursuing here is to partition annual to multidecadal potential intensity variations between global perturbations to the state of the tropical atmosphere, approximated to be in RCE, and local perturbations to that RCE state, approximated to occur under a WTG constraint. To achieve this goal, we start by showing that changes of PI in both RCE and WTG can reasonably be assumed to vary linearly with SST within the domain of observed SST variation. Hereafter, we write $\text{PI} = \text{PI}_0 + \delta\text{PI}$ and $T = T_0 + \delta T$, where PI_0 and T_0 are climatological mean values in a given basin, and δPI and δT are departures from that mean.

Figure 2 shows the change of PI for a given change in SST, with respect to a reference state and for all sensitivity experiments. The domain of the simulations plotted is restricted to $\pm 2\text{ K}$ to outline realistic variations with respect to the control

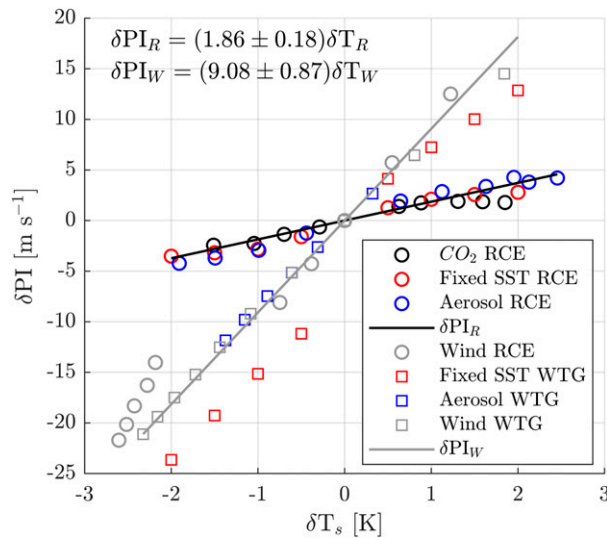


FIG. 2. Plot of δPI against δT for CO_2 (black), fixed SST (red), dust aerosol (blue), and surface wind (gray) sensitivity experiments in RCE (circles) and in WTG (squares). Linear fit for the δPI – δT relations in RCE (black) and in WTG (gray).

case. As one can see, all the experiments fall more or less along two distinct linear slopes (especially near the origin). The shallower slope ($1.8 \text{ m s}^{-1} \text{ K}^{-1}$) is a regression of δPI on δT for all RCE experiments plotted in this figure, except the wind. The steeper slope ($9.0 \text{ m s}^{-1} \text{ K}^{-1}$) is a similar regression for the aerosol, SST, and wind experiments in WTG that are plotted in this figure. The wind experiment was excluded from the RCE case because it behaves similarly to the WTG case, and that remote wind changes should not impact PI much, by comparison to remote SST or radiative forcing changes. The relation between δPI and δT for imposed SST in WTG does not look as linear, because a decrease in SST from the control case leads to the uncoupling of the boundary layer from the troposphere. Those regression slopes are similar to, if somewhat larger than, the reanalysis PI sensitivity (Vecchi and Soden 2007) or other modeled relations (Ramsay and Sobel 2011). To plot this figure and compute the regression, we have selected a similar number of simulations for each sensitivity experiment included, roughly equally spaced to span the δT domain. More precisely, in RCE we have used CO_2 values ranging from 200 to 760 ppm in 40 ppm increments, SST values ranging from 28.6 to 32.6 K in 0.5-K increments, aerosol AOD values ranging from 0 to 0.5 in 0.05 increments, and the wind experiment has not been included in the regression. In WTG, we have used the same SST values as in RCE, aerosol AOD values ranging from 0 to 2 in 0.3 increments and wind values ranging from 3 to 12 m s^{-1} in 1 m s^{-1} increments. The experiments are selected to span realistic temperature variations without using simulations with implausibly large environmental perturbations. For example, even though the WTG aerosol experiment does not span the full $\pm 2\text{-K}$ range, an AOD of less than 0 is impossible and an AOD of more than 2 is implausible, hence we selected

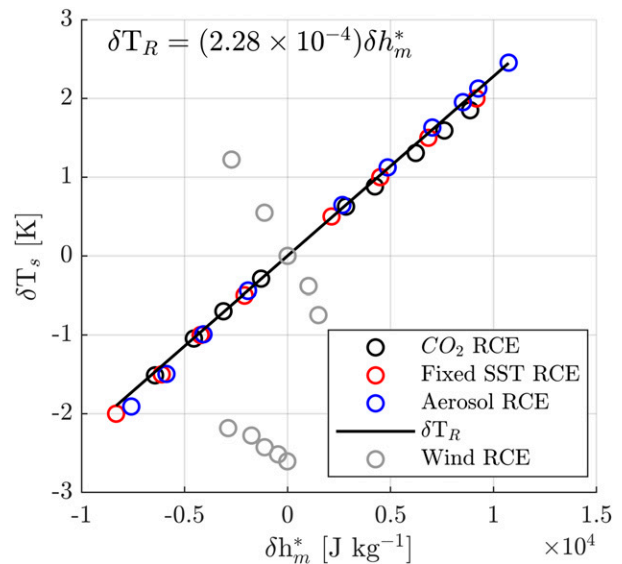


FIG. 3. As in Fig. 1, but in δSSt – δh_m^* space.

simulations within the 0 to 2 range. We note that, as reported in the literature (e.g., Sobel et al. 2019), there are differences in the PI–SST relations between experiments in RCE. For example, RCE PI is more sensitive to SST under an aerosol forcing than under a CO_2 forcing. However, this is not a problem for our model since the difference between the RCE and WTG cases is much larger.

This suggests that we can express PI as two linear functions: one for WTG and the other for RCE perturbations. To achieve this, we need to partition observed SST perturbations between their RCE and WTG components. To do so, we consider the fact that, in theory, under the WTG constraint, changes to the midtropospheric saturation MSE (δh_m^*) should be due to changes in the RCE state. To simplify the problem, we seek a unique function relating δh_m^* to δT_R , the SST change in RCE.

Figure 3 shows the RCE sensitivity experiments introduced earlier, plotted in δT – δh_m^* space. The WTG simulations are omitted as h_m^* does not change with SST in WTG. Second, we note that most RCE simulations fall on a single profile that is quite linear over the plotted domain. That profile does not vary much between sensitivity experiments. The regression coefficient for δPI and δT for all RCE experiments but the wind is about $2.28 \times 10^{-4} \text{ kg K J}^{-1}$. Finally, we note that h_m^* changes nonmonotonically with SST in the RCE–wind sensitivity experiment. This is due to the model transitioning between two stable configurations and is a consequence of using a single column model. Both configurations exhibit negative correlations between δT and δh_m^* , which may be due to the fact that, in the simulations, a wind increase leads to a decrease of SST while increasing the moisture (and hence greenhouse gas) content of the atmosphere. This in turn seems to lead to a warmer atmosphere despite the colder surface. We circumvent those considerations by noticing that local changes in winds are much larger than tropics-wide changes (which is supported by reanalysis) and by neglecting the wind contribution to RCE

changes altogether. This leaves us with two linear slopes for the $\delta\text{PI}-\delta T$ relation in RCE and WTG and one for the $\delta T-\delta h_m^*$ relation in RCE.

a. A linear model informed by theory and a single-column model

To develop a linear model for δPI as a function of δT and δh_m^* , we first partition δT , the total SST change, between SST changes in RCE, and a perturbation with respect to the RCE state. We pose

$$\delta T = \delta T_R + \delta T_W, \quad (14)$$

where δT_R is the SST change in RCE, and δT_W is the remainder of the total SST change. Then, δT_R can be related to δh_m^* by posing

$$\delta T_R = C_m \delta h_m^*, \quad (15)$$

where m refers to the midtroposphere and, from Fig. 3, we have $C_m = 2.28 \times 10^{-4} \text{ kg K J}^{-1}$ as a constant. Defined in that way, the PI sensitivity to δT_R should be the PI sensitivity to SST in RCE. The remainder δT_W , which is given by

$$\delta T_W = \delta T - C_m \delta h_m^*, \quad (16)$$

is not associated with any change in h_m^* and will control PI as if in WTG, hence the subscript W . Adding in the linear coefficients for PI sensitivity in RCE and WTG from Fig. 2, we introduce the fundamental partition we want to make:

$$\delta\text{PI} = C_R \delta T_R + C_W \delta T_W, \quad (17)$$

where $C_R = 1.8 \text{ m s}^{-1} \text{ K}^{-1}$ and $C_W = 9.0 \text{ m s}^{-1} \text{ K}^{-1}$, corresponding in theory to the sensitivities given by Eqs. (8) and (12). The quantity δT can be readily retrieved from models or observations. The quantity δh_m^* is a function of temperature and geopotential on a given pressure level, and can also be retrieved from reanalysis products. Combining the equations, we obtain

$$\delta\text{PI} = C_R C_m \delta h_m^* + C_W (\delta T - C_m \delta h_m^*), \quad (18)$$

where the first term on the RHS is the contribution to PI changes from changes to the RCE state, and the second term is the contribution from changes in the WTG state. Rearranging to combine the predictors we get

$$\delta\text{PI} = C_m (C_R - C_W) \delta h_m^* + C_W \delta T. \quad (19)$$

Here the physical interpretation of the two terms changes to provide further insight. Since $C_W > C_R$ and $C_m > 0$, we can see that the coefficient of the first term is negative, which reflects the fact that a positive δh_m^* , in the absence of a compensating increase in SST, will cause a decrease in PI. Conversely, the second coefficient is the large positive increase in PI that occurs when SST increases locally, while the midtroposphere remains fixed. The coefficients for this form of the equation can be obtained from both the SCM and from a linear fit based on reanalysis data, and compared to verify the model.

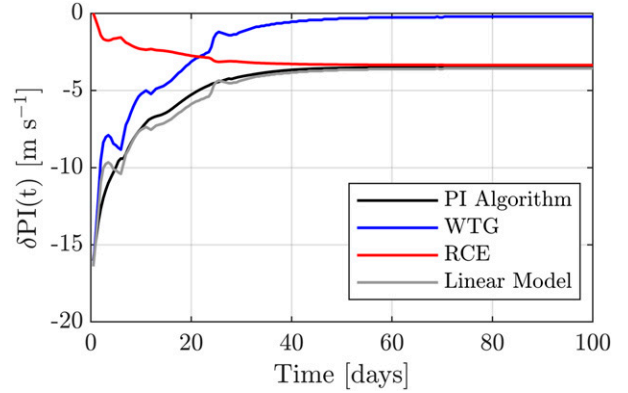


FIG. 4. Evolution of PI toward RCE in a fixed SST single-column simulation, when SST is perturbed by -2 K . Time series of algorithm PI (black) and linear model PI (gray) and the equilibrium (red) and transient (blue) components of linear model PI. The red and the blue lines correspond respectively to the first and second terms on the RHS of Eq. (17), respectively.

b. Unsteadiness

We note that the component of SST or PI we called “WTG” is for now just a component that departs from the RCE state and does not entail that the SST perturbation is local in space. This will have to be verified using reanalysis data. Consider the application of the linear model to the time-dependent evolution of single-column simulation toward RCE. If our linear model is correct, we should be able to reproduce PI variations based only on the departure of δT and δh_m^* from the initial conditions. For example, let us consider the evolution of the fixed SST simulation where SST is perturbed by -2 K . Initially, as shown by Fig. 4, we have $\delta\text{PI} = C_W \delta T_W$ and the PI perturbation does not reflect any RCE change. For this plot, we have arbitrarily taken $C_W = 8.2 \text{ m s}^{-1} \text{ K}^{-1}$ for best results. This is slightly smaller than the value of the PI sensitivity C_W obtained by regression over all WTG simulations, but it is still within the confidence interval. Our only goal here is to show that PI can be represented at each point in the evolution by a linear model. As time goes on, the RCE component increases and the transient component decreases. At the end, as the system has reached RCE, $\delta\text{PI} = C_R \delta T_R$, and there is no more departure from RCE.

In between the initial time and equilibrium, δT_R increases and δT_W decreases, and if we substitute both time-dependent values in Eq. (17), we can reproduce the evolution of PI as captured by the Bister and Emanuel (2002) algorithm.

This means that a linear model cannot, on its own, distinguish between WTG perturbations and transience, but it can identify the part of SST variations that is coherent with an RCE state. To show that the remainder of SST variations corresponds to a state in WTG, we need to apply the linear model to reanalysis data, and show that the use of a tropical average value of δh_m^* is sufficient to capture PI variations.

6. Application to reanalysis products

To verify that the linear model captures PI variations, we apply it to ERA5 (Hersbach et al. 2020) monthly averaged data.

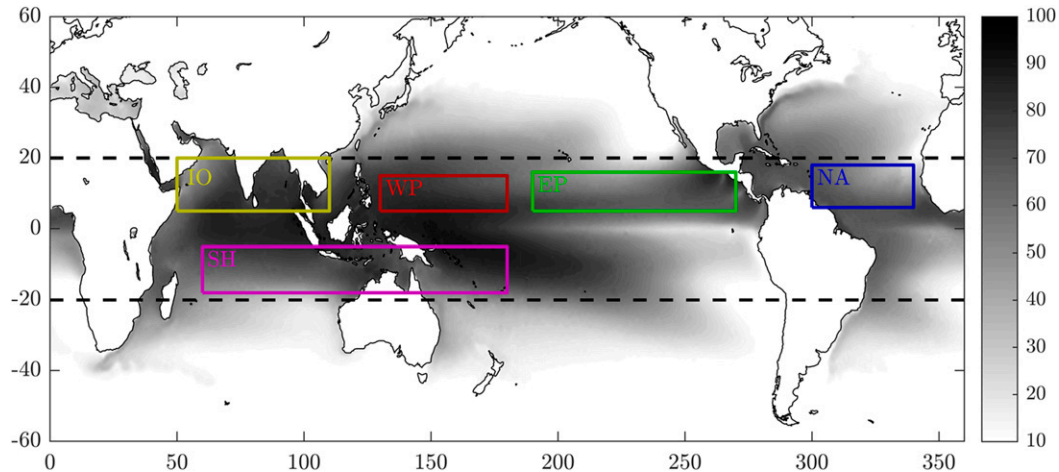


FIG. 5. Tropical ocean basins for PI analysis plotted over a map of average PI in ERA5 from 1979 to 2018. SST is averaged seasonally and over each basin: North Atlantic (NA; blue), east Pacific (EP; green), west Pacific (WP; red), Indian Ocean (IO; yellow), and a large basin for the Southern Hemisphere (SH; magenta). The seasons are defined as follows: the NA TC season is August–October, the EP TC season is June–September, the WP TC season is July–November, the IO TC season is April–November, and the SH TC season is January–May. Midlevel saturation MSE is averaged over the area enclosed by the two black dashed lines and is averaged over the TC seasons of each basin separately.

The resulting linear model PI (LPI) variations are then compared to a reference PI dataset computed using ERA5 data and pyPI (Gilford 2020), a Python package for the nonlinear iterative algorithm developed by Bister and Emanuel (2002). The PI dataset was graciously provided by Daniel Gilford. In this dataset, which is most appropriate for the study of the maintenance of TCs, the highest value of PI is selected when a decoupled BL results in a multivalued PI. As we will show, this causes linear PI variability to be underestimated in ocean basins where decoupling occurs frequently. To compute LPI for each basin, the saturation MSE predictor δh_m^* , which is assumed to be uniform over the tropics, is averaged over the 600-hPa pressure level from 20°N to 20°S and at all latitudes, and the sea surface temperature predictor δT is averaged over each tropical ocean basin separately. The averaging of PI and SST excludes land in all basins. As shown in Fig. 5, we define five ocean basins in total; the North Atlantic (NA), eastern North Pacific (EP), western North Pacific (WP), northern Indian Ocean (IO), and a single large basin for the Southern Hemisphere (SH), in the Pacific. To make sure that the quantities computed are relevant to TC activity, PI variations are computed from predictors averaged over the tropical storm season of each basin respectively.

We then apply the linear model to the spatially and seasonally averaged predictors to compute one value of PI per basin per year. In the reference PI dataset provided by Daniel Gilford, pyPI is applied to ERA5 monthly averaged SST and vertical profiles of p , T , and r at each latitude–longitude point. The PI dataset is also averaged over each basin and over the corresponding tropical storm season. A comparison between LPI and the algorithm PI allows one to evaluate the linear model, but to ensure that our SCM-derived coefficients are valid, we also compute a linear fit of the algorithm PI to our two LPI predictors, δT and δh_m^* . This is equivalent to employing

Eq. (19), with the coefficients of both predictors determined statistically rather than numerically. To sum up we are left with three ways to compute potential intensity: LPI, algorithm PI, and linear fit PI.

Figure 6a shows that, in the tropical North Atlantic main development region (MDR), LPI captures very well the variations of the algorithm PI ($R = 0.97$) and is almost indistinguishable from the linear fit PI. This shows that δT_s and δh_m^* are a good choice of predictors, and also that the SCM-derived coefficients are very close to the linear fit coefficients (as we will see later). This suggests that we can interpret past PI variations in light of the SCM-derived coefficients, which provide physical meaning. In addition, the excellent performance of the linear model in capturing the interannual algorithm PI variations suggests that the nonlinearities and the iterative process involved in the algorithmic computation have a fairly small impact on PI sensitivity (or cancel out), at least over the range of conditions tested in this paper.

In Fig. 6b, we have used Eqs. (15) and (16) to partition the variations of SST into WTG and RCE contributions in the MDR. We can see that while the variations of δT_R have been smaller than those of δT_W over the last 40 years, the magnitudes are comparable. δT_R exhibits a positive trend in time that is likely due to global warming. The detrended variability in δT_R correlates well with the Niño-3.4 index ($R = 0.67$ with a 3-month lag and $R = 0.5$ without any lag, not shown) because large-scale ocean heat flux has an important influence on the tropical atmosphere. Determining the causes of δT_W , or δPI_W , variability exceeds the scope of the present study and will be the topic of a subsequent paper. Causes can include aerosol radiative forcings, wind-induced surface heat exchange, and ocean circulations like the Atlantic meridional overturning circulation.

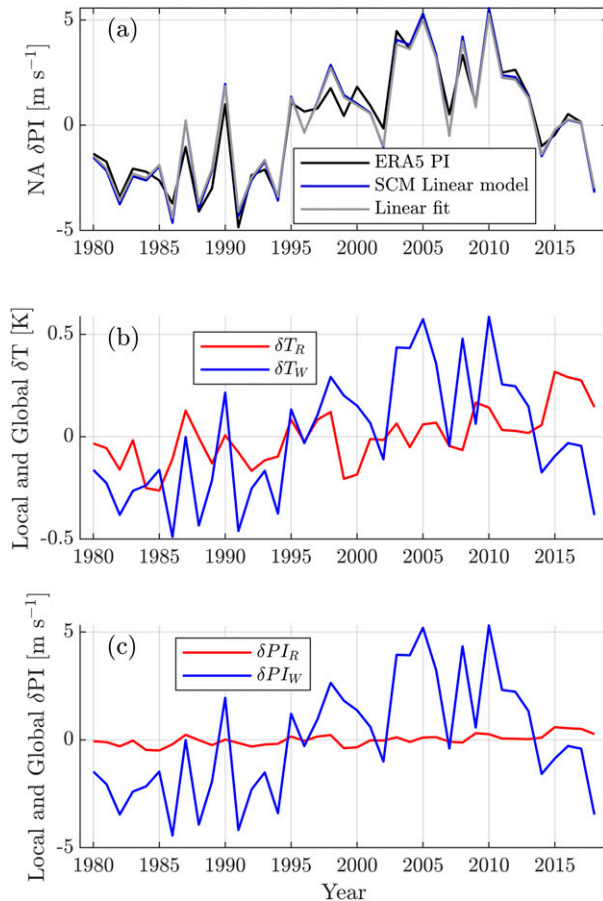


FIG. 6. (a) Time series computed over the North Atlantic MDR and ASO of “true” algorithm δPI (black), of δPI estimated using the SCM-derived linear model (blue), and of δPI estimated using an in-sample linear fit on δT and δh_m^* (gray). (b) Time series of SST change (δT) over the MDR and averaged over hurricane season partitioned between its RCE (red) and WTG (blue) components. (c) Partition of δPI averaged over the MDR and ASO, between its RCE (red) and WTG (blue) components.

Finally, in Fig. 6c we look at the partition of PI variations into global (δPI_R) and local (δPI_W) contributions. Clearly, in the MDR, the global contribution to PI variations is negligible compared to the local contribution, in the last 40 years. However, even though δPI_R is small, we still need to know δT_R in order to be able to estimate δT_W and have an accurate estimate of δPI_W , which dominates the variability. Note that the fact that global effects on PI are small in the Atlantic MDR does not mean that they are small poleward of the tropics.

a. Other basins

Figure 7 shows the coefficient of determination (R^2) of the linear model in all ocean basins; as we can see, LPI reproduces algorithm PI well in all basins. The basin with the smallest R^2 is the eastern North Pacific with 80% of the interannual PI variance captured by LPI. The maximum variance explained by the model is 95%, in the North Atlantic. It is not surprising

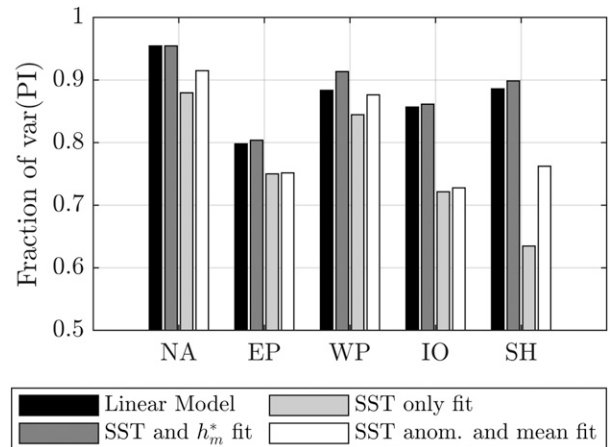


FIG. 7. Coefficient of determination between algorithm PI and LPI (black bars), between algorithm PI and a statistical fit based on SST and h_m^* (dark gray bars), between algorithm PI and SST (pale gray bars), and between algorithm PI and a statistical fit based on mean SST and SST anomaly (white bars), for each basin.

that the linear model works best in the North Atlantic MDR since the simulations from which the model coefficients are derived vary around a control simulation designed to resemble the conditions over that basin. Figure 7 also shows the fraction of variance that can be explained by a statistical fit of PI to SST and h_m^* . As we can see, the statistical fit improves little upon the SCM-derived linear model, ranging from no improvement in the NA to a 3% improvement in the WNP. This suggests that the SCM-derived coefficients are close to the statistical fit coefficients, which will be verified in the next section.

To illustrate the relative roles of global and local influences, Fig. 8 shows the partition of SST between local and global contributions, in the four additional basins. Since the global contribution to SST depends only on δh_m^* , which is averaged over the whole tropics and is common to all basins, the only difference between the δT_R time series across different basins is the averaging season. If two basins had the same TC season, they would have the same δT_R every year. In basins that have much smaller SST variability than the NA, like the IO or the SH, the local contribution to SST changes δT_W is smaller than δT_R . In the SH basin δT_R very clearly shows El Niño events, notably in 1983, 1998, 2010, and 2016, because the averaging includes the months of January and February, during which the events tend to reach peak magnitude. We have not included a figure showing the partition between δPI_R and δPI_W for all basins because the information can be retrieved by multiplying δT_R by $C_R = 1.8 \text{ m s}^{-1} \text{ K}^{-1}$ and δT_W by $C_W = 9.0 \text{ m s}^{-1} \text{ K}^{-1}$. The time series of δPI_R is similar across all basins and is everywhere smaller than δPI_W with the difference being largest in basins with large SST variability like the ENP.

b. Reanalysis coefficients

So far we have shown that LPI correlates well with algorithm PI across all basins. Next, we want to show that the coefficients derived from the SCM simulations have a physical meaning

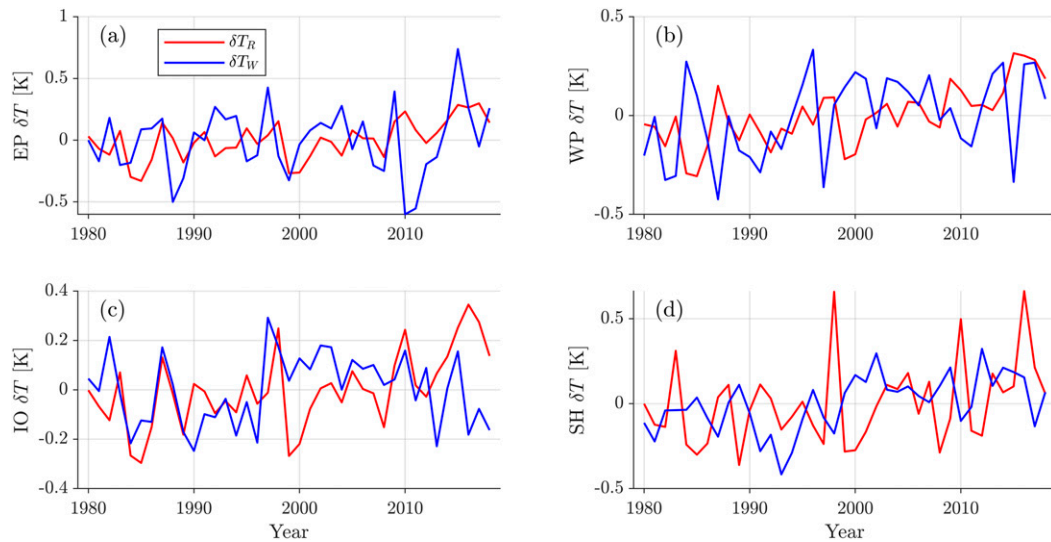


FIG. 8. Time series of SST change (δT) averaged over each basin and the corresponding TC season partitioned between their RCE (red) and WTG (blue) components for (a) the eastern North Pacific, (b) the western North Pacific, (c) the northern Indian Ocean, and (d) the Southern Hemisphere basin.

that can be used to interpret PI variations in reanalysis data. To do so, we obtain linear fit coefficients by regressing PI on δT and δh_m^* in ERA5. This yields a formula of the form $\delta \text{PI} = C_1 \delta T + C_2 \delta h_m^*$. This linear fit PI is plotted in gray in Fig. 6a and unsurprisingly also captures PI variation very well. Comparison of the linear fit with Eq. (19) yields that, if the SCM model assumptions are valid, then $C_1 = C_W$ and $C_2 = C_m(C_R - C_W)$. Figure 9a shows coefficient C_W derived from SCM simulations (same as in Fig. 2) along with coefficient $C_1 = C_W$ for each ocean basin, in black. The regression coefficients are plotted with 95% confidence intervals where intervals are computed using the Wald method. For example, our 95% confidence interval on the WTG coefficient is given by $C_W \pm \sigma(C_W) t_{(1-0.05/2, n-2)}$ where $\sigma(C_W)$ is the standard error of the estimate of the coefficient, and $t_{(1-0.05/2, n-2)}$ is the 97.5th percentile of the t distribution with $n - 2$ degrees of freedom (where n is the number of points). This shows that, except for EP, the coefficients from all ocean basins are indistinguishable from the SCM-derived coefficient. The reason why EP has a different coefficient will be explained below. The red \times markers denote analytical estimates for coefficient C_W , obtained from the control simulation and each basin, by applying Eq. (8). For both the SCM simulation and the NA basin, the empirical estimates are just slightly lower than the theoretical estimates, while for the EP it is much lower. For the WP, IO and SH basins, both the empirical and theoretical estimates are statistically indistinguishable. The analytical estimates are similar for all basins and for the SCM simulation, with less than a $1 \text{ m s}^{-1} \text{ K}^{-1}$ difference between the highest and the lowest value. The good agreement between the SCM coefficient and the empirical and theoretical coefficients over each basin suggests that, in both the SCM and reanalysis data, the QE assumption is satisfied, or at least that the departure from QE is not very climate sensitive. Figure 9b shows the combination of coefficients $C_m(C_R - C_W)$ derived from SCM simulations along with coefficient $C_2 = C_m(C_R - C_W)$

for each ocean basin. Although there is a lot of uncertainty on the coefficients in some basins, like in the EP, all uncertainty bounds overlap so that all coefficients are indistinguishable from a value of about $-1.5 \text{ m kg s}^{-1} \text{ J}^{-1}$. The negative value implies that, for an unchanged SST, if h_m^* increases, potential intensity must decrease.

In Fig. 9a, we have also plotted a coefficient of linear regression of PI on SST alone such that $\delta \text{PI} \approx C_3 \delta T$. Since δT is positively correlated with δh_m^* (not shown), the coefficient C_3 must be smaller than C_W . If the correlation was perfect we should have $C_3 \approx C_R$, so C_R and C_W are essentially lower and upper bounds on C_3 . In our Fig. 9a, the SH basin, which has the largest correlation between δh_m^* and δT has the largest difference between C_3 and C_R , and conversely for the EP basin, which has the smallest correlation. This is worth pointing out because it contextualizes the use of SST alone as a predictor of tropical cyclone intensity: it only works well if that SST is independent of midtropospheric conditions. To support this, we look at the coefficients of determination for SST alone in Fig. 7 and notice they are always smaller than the R^2 of the SCM-derived model, which also includes δh_m^* . The difference is again largest in the SH basin, where the correlation between δh_m^* and δT is strongest.

7. Discussion

Our results outline the importance of coefficient C_W in determining the magnitude of PI variations associated with a given SST perturbation. In addition, C_m allows one to define that perturbation based on the mean tropical state and is also important. On the other hand, in the Atlantic, C_R is not very important up to multidecadal time scales because RCE PI changes account only for a small fraction of the total. We want to emphasize that this may not hold at longer time scales. The local coefficients C_W found here are larger than those presented in Vecchi and Soden (2007), which relied on fitting

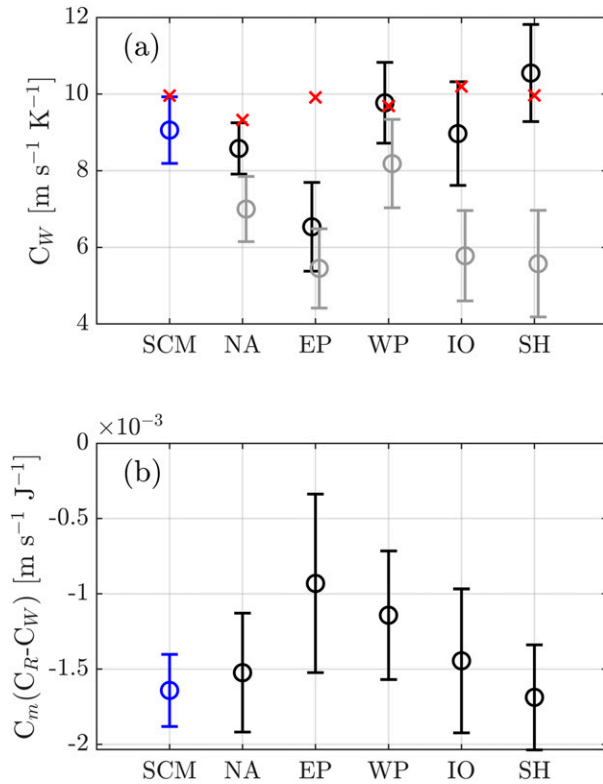


FIG. 9. (a) Linear model coefficients C_W derived from the SCM simulations (blue; SCM label) and derived from ERA5 PI regression on both δT and δh_m^* (black; basin labels), analytical estimates of C_W using Eq. (8) (red \times), and coefficient of ERA5 PI regression on δT only (gray). (b) Combination of linear coefficients $C_m(C_R - C_W)$ derived from the SCM simulations (blue; SCM label) and derived from ERA5 PI regression (black; basin labels). The error bars denote 95% confidence interval on the regression coefficients.

algorithm PI to a temperature anomaly computed with respect to the tropical average at each time step. This method is the equivalent to setting $\delta T_W = \delta T - \delta \bar{T}$, where $\delta \bar{T}$ are tropical mean SST changes. In addition, it assumes $\delta \text{PI}_R = C_R \delta \bar{T} \approx 0$, and we indeed have found δPI_R to be small. So the main difference lies in the assumption that $\delta \bar{T}$ is representative of δh_m^* , which depends not only on SST, but on the degree of coupling of the sea surface to the atmosphere. We illustrate this assumption in Fig. 10, where we show a time series $\delta \bar{T}$ averaged over the tropical North Atlantic hurricane season, along with $C_m \delta h_m^*$ averaged over the same season. As we can see, in general, $\delta \bar{T} \propto \delta h_m^*$, with a correlation coefficient $R = 0.81$. The linear regression coefficient between both variables over the last 40 years is $(2.69 \pm 0.64) \times 10^{-4} \text{ kg K J}^{-1}$, which is indistinguishable from the value of the coefficient C_m obtained from the SCM simulations. This is interesting because the value of C_m , and by extension that of C_R , are expected to depend not only on the atmospheric cooling rate, but also sensitively on the level of coupling between the sea surface and the boundary layer. We assumed this coupling to be fixed in the derivation of Eq. (11) and in the computation of C_m and C_R from simulation

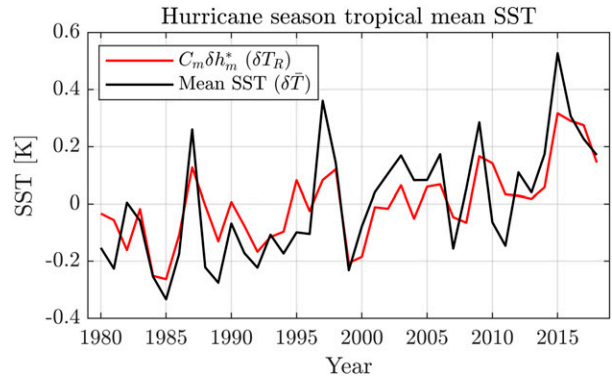


FIG. 10. Comparison between tropical mean SST (black) and an estimate of SST representative of global changes by our linear model (red). Both quantities are averaged over the North Atlantic hurricane season.

results, where we left the wind experiment out of the regression. Hence this result suggests that large-scale changes in coupling, for example due to global trade wind changes, were not very important on multidecadal time scales in the last 40 years. It also suggests that the a priori assumption we made, namely that changes in surface winds could be excluded from the computation of C_m and C_R , is valid, at least for the period considered. However, we notice that fairly large departures between $\delta \bar{T}$ and $C_m \delta h_m^*$ occur during El Niño years, where large changes in the pattern of SST are associated with changes in the level of coupling between the ocean and the atmosphere, on a large scale. Hence, on multidecadal time scales, the assumption $\delta \bar{T} \propto \delta h_m^*$ seems a good one, but it seems less robust when aiming to capture the effects of interannual variability on PI.

Next, we compare methods based on tropical average and perturbation to the method introduced here. In Fig. 7, we show the fraction of PI variance that can be explained by a statistical fit of PI to both mean SST ($\delta \bar{T}$) and SST anomaly ($\delta T - \delta \bar{T}$). As we can see, the linear model introduced here explains systematically more variance than the simple fit based on SST mean and anomaly. However, we also note that the fit based on SST mean and anomaly explains more variance than the fit based on basin SST alone, which does not account for large-scale changes. As expected, the difference is most important in the SH basin, where basin SST is most correlated with tropical mean SST.

a. The eastern Pacific

The EP basin stands against an oceanic boundary with lots of cold water upwelling, which causes the BL to decouple from the free troposphere much more frequently than occurs in other basins. This decoupling causes PI to be multivalued and causes the high PI value to vary nonmonotonically in temperature, increasing for a while as temperature decreases and the boundary layer decouples, before decreasing again. This nonmonotonicity results in a lower PI variability than predicted by the SCM linear model over the same range of temperatures. In other words, this is the reason why the EP

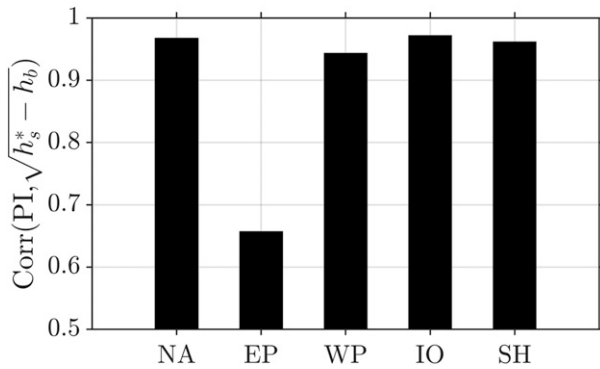


FIG. 11. Correlation coefficients between PI and the square root of thermodynamic disequilibrium for each basin.

linear fit C_W coefficient is considerably lower than the linear model C_W in Fig. 9a.

To show that this is the case, we consider that the PI computation algorithm (e.g., Gilford 2020) is based on the equivalence between thermodynamic disequilibrium and the difference between environmental CAPE and saturation CAPE. The algorithm also includes a nonlinear operation that specifies that the environmental CAPE cannot be less than zero for the purpose of the PI computation. This condition is usually applied when the boundary layer decouples; when applied, it breaks the equivalence between thermodynamic disequilibrium and the difference of CAPEs. Hence, when the boundary layer decouples, the square root of the thermodynamic disequilibrium becomes less correlated with PI computed with the algorithm. This tells us that frequent boundary layer decoupling should decrease the correlation between algorithm PI and the square root of the thermodynamic disequilibrium, which we can test. Figure 11 shows this correlation for all basins and outlines that the BL decouples far more often in the EP than in other basins. Indeed, the correlations are about 0.95 for all basins except the EP, where it is 0.65.

b. Applications

The goal of this study is to provide a framework for quantifying the causes of PI variability in the tropics. So far, we have shown that PI variations are well captured by a novel linear model based on two simple and intuitive predictors. This linearity of PI, along with the fact that the model coefficients have a clear physical meaning, constitutes the basis of our framework. First, the linearity of PI will allow us to study the different local influences on SST perturbations independently from one another and then convert the SST perturbations corresponding to each influence on PI perturbations. For example, if it is known that dust aerosol forcing accounts for twice as much TNA SST variability as ocean heat flux convergence, then it also accounts for twice as much PI variability. Then, the physical meaning of the model coefficients allows us to obtain information on the cause of PI changes since SST and PI can be partitioned between an RCE component, corresponding to large-scale changes to the tropical atmosphere, and a WTG departure from those large-scale changes.

The coefficient C_W derives from Clausius–Clapeyron and could apply to any departure from RCE, but the fact that the tropical average h_m^* predictor greatly improves the linear model confirms that these departures occur in WTG. Throughout all basins, PI variations are dominated by WTG variations, at least over the last 40 years, which suggests that changes in SST patterns due to global change might be more important for PI and TC activity than the changes in global mean temperature themselves. This highlights that any small domain simulation or idealized model that attempts to capture the response of SST and PI to local parameter changes should be constrained by WTG. The coefficient C_m , however, is a fundamental property of Earth’s atmosphere that can be related to atmospheric cooling and indicates the slope of the relation between midlevel saturation entropy and SST. This coefficient outlines why PI is relatively insensitive to global warming over the period considered in the study. Because the changes of surface coupling and poleward energy transport were not large enough to greatly influence C_m over the last 40 years, an SCM was sufficient to estimate its value. However, to capture the response of PI to global change over a much longer period a global climate model is probably more appropriate, since the SCM can provide no insight on surface coupling or poleward energy transport.

We note that those coefficients were derived from equilibrium simulations but do not actually require a steady state to be applicable. For example, if large-scale oceanic fluxes like those due to ENSO increase rapidly and heat up the atmosphere, small remote basins like TNA will see a drop in PI before their temperature adjusts, and an increase afterward. Conversely, rapid changes in large coupled basin SST will result in large basin PI changes before the atmosphere has time to adjust, and more modest ones afterward. For example, the 2015/16 El Niño event is clearly visible in Fig. 8, where there is a large increase in WTG-like perturbation temperature in the EP basin, and a correspondingly large decrease in the WP basin. In those plots, the fraction of SST that correlates with h_m^* is not very large, outlining that the atmosphere has not adjusted yet to these perturbed SSTs during the boreal summer. Early the next year, during the averaging season of the SH in the austral summer, we can see that the RCE temperature component is much larger while the absolute anomalous component is much smaller than in the two other basins, earlier in the year. This suggests that the SSTs are closer to equilibrium with the atmosphere then, in the SH basin.

8. Conclusions

In this study, we introduced a new linear model for potential intensity, based on SCM simulations and on the sensitivities of PI to SST in atmospheres in RCE and under the WTG constraint. The model coefficients are derived from a control simulation designed to be similar to Atlantic conditions, and from a set of sensitivity experiments to CO_2 in RCE and to dust optical depth, imposed SST changes, and surface winds, in RCE and under WTG constraints. The resulting linear model allows us to partition SST and PI changes into local and global components, and explains up to 95% of the interannual to multidecadal basin-averaged seasonal PI variance. The basin

where the model works best is the NA, which may be due to the fact that the control simulation was designed to have similar conditions as the NA. The basin where the model captures the least variance is the EP, which may be due to cold water upwelling intermittently decoupling the boundary layer from the midlevels, and decreasing PI sensitivity. Apart from the EP, the linear model coefficients derived from SCM simulations are indistinguishable in all basins from linear fit coefficients derived using ERA5.

Future work will demonstrate applications of this framework, including estimating the relative contributions of various mechanisms to the historical PI variations, and quantifying the thermodynamic effect of ENSO on Atlantic hurricane activity. In addition, the results suggest that it would be interesting to evaluate the sensitivity of PI and SST to direct and indirect dust aerosol effects, and the associated cloud feedbacks, in WTG-constrained cloud-resolving model simulations.

Acknowledgments. This work was supported by NSF Grant AGS-1906768. The authors thank Daniel Gilford for providing the ERA5 PI dataset that has been used as a reference in this study. Support for the Twentieth Century Reanalysis Project version 3 dataset is provided by the U.S. Department of Energy, Office of Science Biological and Environmental Research (BER), by the National Oceanic and Atmospheric Administration Climate Program Office, and by the NOAA Physical Sciences Laboratory.

REFERENCES

- Arakawa, A., and W. H. Schubert, 1974: Interaction of a cumulus cloud ensemble with the large-scale environment, part I. *J. Atmos. Sci.*, **31**, 674–701, [https://doi.org/10.1175/1520-0469\(1974\)031<0674:IOACCE>2.0.CO;2](https://doi.org/10.1175/1520-0469(1974)031<0674:IOACCE>2.0.CO;2).
- Bister, M., and K. A. Emanuel, 1998: Dissipative heating and hurricane intensity. *Meteor. Atmos. Phys.*, **65**, 233–240, <https://doi.org/10.1007/BF01030791>.
- , and —, 2002: Low frequency variability of tropical cyclone potential intensity 1. Interannual to interdecadal variability. *J. Geophys. Res.*, **107**, 4801, <https://doi.org/10.1029/2001JD000776>.
- Bony, S., and K. A. Emanuel, 2001: A parameterization of the cloudiness associated with cumulus convection; evaluation using TOGA COARE data. *J. Atmos. Sci.*, **58**, 3158–3183, [https://doi.org/10.1175/1520-0469\(2001\)058<3158:APOTCA>2.0.CO;2](https://doi.org/10.1175/1520-0469(2001)058<3158:APOTCA>2.0.CO;2).
- Booth, B. B., N. J. Dunstone, P. R. Halloran, T. Andrews, and N. Bellouin, 2012: Aerosols implicated as a prime driver of twentieth-century North Atlantic climate variability. *Nature*, **484**, 228–232, <https://doi.org/10.1038/nature10946>.
- Bryan, G. H., and R. Rotunno, 2009: Evaluation of an analytical model for the maximum intensity of tropical cyclones. *J. Atmos. Sci.*, **66**, 3042–3060, <https://doi.org/10.1175/2009JAS3038.1>.
- Dunstone, N., D. Smith, B. Booth, L. Hermanson, and R. Eade, 2013: Anthropogenic aerosol forcing of Atlantic tropical storms. *Nat. Geosci.*, **6**, 534–539, <https://doi.org/10.1038/ngeo1854>.
- Emanuel, K. A., 1986: An air–sea interaction theory for tropical cyclones. Part I: Steady-state maintenance. *J. Atmos. Sci.*, **43**, 585–605, [https://doi.org/10.1175/1520-0469\(1986\)043<0585:AASITF>2.0.CO;2](https://doi.org/10.1175/1520-0469(1986)043<0585:AASITF>2.0.CO;2).
- , 1988: The maximum intensity of hurricanes. *J. Atmos. Sci.*, **45**, 1143–1155, [https://doi.org/10.1175/1520-0469\(1988\)045<1143:TMIOH>2.0.CO;2](https://doi.org/10.1175/1520-0469(1988)045<1143:TMIOH>2.0.CO;2).
- , 2000: A statistical analysis of tropical cyclone intensity. *Mon. Wea. Rev.*, **128**, 1139–1152, [https://doi.org/10.1175/1520-0493\(2000\)128<1139:ASAOTC>2.0.CO;2](https://doi.org/10.1175/1520-0493(2000)128<1139:ASAOTC>2.0.CO;2).
- , 2007: Environmental factors affecting tropical cyclone power dissipation. *J. Climate*, **20**, 5497–5509, <https://doi.org/10.1175/2007JCLI1571.1>.
- , and M. Živković-Rothman, 1999: Development and evaluation of a convection scheme for use in climate models. *J. Atmos. Sci.*, **56**, 1766–1782, [https://doi.org/10.1175/1520-0469\(1999\)056<1766:DAEOAC>2.0.CO;2](https://doi.org/10.1175/1520-0469(1999)056<1766:DAEOAC>2.0.CO;2).
- , and A. Sobel, 2013: Response of tropical sea surface temperature, precipitation, and tropical cyclone-related variables to changes in global and local forcing. *J. Adv. Model. Earth Syst.*, **5**, 447–458, <https://doi.org/10.1002/jame.20032>.
- Evan, A. T., and S. Mukhopadhyay, 2010: African dust over the northern tropical Atlantic: 1955–2008. *J. Appl. Meteor. Climatol.*, **49**, 2213–2229, <https://doi.org/10.1175/2010JAMC2485.1>.
- , G. R. Foltz, D. Zhang, and D. J. Vimont, 2011: Influence of African dust on ocean–atmosphere variability in the tropical Atlantic. *Nat. Geosci.*, **4**, 762–765, <https://doi.org/10.1038/ngeo1276>.
- , C. Flamant, M. Gaetani, and F. Guichard, 2016: The past, present and future of African dust. *Nature*, **531**, 493–495, <https://doi.org/10.1038/nature17149>.
- Fouquart, Y., and Coauthors, 1980: Computations of solar heating of the Earth’s atmosphere: A new parameterization. *Beitr. Phys. Atmos.*, **53**, 35–62.
- Gilford, D. M., 2020: pyPI (v1.3): Tropical cyclone potential intensity calculations in Python. *Geosci. Model Dev.*, **14**, 2351–2369, <https://doi.org/10.5194/gmd-14-2351-2021>.
- , S. Solomon, and K. A. Emanuel, 2017: On the seasonal cycles of tropical cyclone potential intensity. *J. Climate*, **30**, 6085–6096, <https://doi.org/10.1175/JCLI-D-16-0827.1>.
- Hersbach, H., and Coauthors, 2020: The ERA5 global reanalysis. *Quart. J. Roy. Meteor. Soc.*, **146**, 1999–2049, <https://doi.org/10.1002/qj.3803>.
- Jeevanjee, N., and D. M. Romps, 2018: Mean precipitation change from a deepening troposphere. *Proc. Natl. Acad. Sci. USA*, **115**, 11 465–11 470, <https://doi.org/10.1073/pnas.1720683115>.
- Mann, M. E., and K. A. Emanuel, 2006: Atlantic hurricane trends linked to climate change. *Eos, Trans. Amer. Geophys. Union*, **87**, 233–241, <https://doi.org/10.1029/2006EO240001>.
- Merlis, T., R. Rousseau-Rizzi, and N. Jeevanjee, 2021: CAPE-based derivation of approximate tropical cyclone potential intensity formula. <https://doi.org/10.1002/essoar.10506988.1>.
- Morcrette, J.-J., 1991: Radiation and cloud radiative properties in the European Centre for Medium Range Weather Forecasts forecasting system. *J. Geophys. Res.*, **96**, 9121–9132, <https://doi.org/10.1029/89JD01597>.
- O’Gorman, P. A., and T. Schneider, 2008: The hydrological cycle over a wide range of climates simulated with an idealized GCM. *J. Climate*, **21**, 3815–3832, <https://doi.org/10.1175/2007JCLI2065.1>.
- Ramsay, H. A., and A. H. Sobel, 2011: Effects of relative and absolute sea surface temperature on tropical cyclone potential intensity using a single-column model. *J. Climate*, **24**, 183–193, <https://doi.org/10.1175/2010JCLI3690.1>.
- Rousseau-Rizzi, R., and K. Emanuel, 2019: An evaluation of hurricane superintensity in axisymmetric numerical models. *J. Atmos. Sci.*, **76**, 1697–1708, <https://doi.org/10.1175/JAS-D-18-0238.1>.
- Sobel, A. H., and C. S. Bretherton, 2000: Modeling tropical precipitation in a single column. *J. Climate*, **13**, 4378–4392, [https://doi.org/10.1175/1520-0442\(2000\)013<4378:MTPIAS>2.0.CO;2](https://doi.org/10.1175/1520-0442(2000)013<4378:MTPIAS>2.0.CO;2).
- , S. J. Camargo, and M. Previdi, 2019: Aerosol versus greenhouse gas effects on tropical cyclone potential intensity and

- the hydrologic cycle. *J. Climate*, **32**, 5511–5527, <https://doi.org/10.1175/JCLI-D-18-0357.1>.
- Strong, J. D., G. A. Vecchi, and P. Ginoux, 2015: The response of the tropical Atlantic and West African climate to Saharan dust in a fully coupled GCM. *J. Climate*, **28**, 7071–7092, <https://doi.org/10.1175/JCLI-D-14-00797.1>.
- , —, and —, 2018: The climatological effect of Saharan dust on global tropical cyclones in a fully coupled GCM. *J. Geophys. Res. Atmos.*, **123**, 5538–5559, <https://doi.org/10.1029/2017JD027808>.
- Vecchi, G. A., and B. J. Soden, 2007: Effect of remote sea surface temperature change on tropical cyclone potential intensity. *Nature*, **450**, 1066–1070, <https://doi.org/10.1038/nature06423>.
- Villarini, G., and G. A. Vecchi, 2013: Projected increases in North Atlantic tropical cyclone intensity from CMIP5 models. *J. Climate*, **26**, 3231–3240, <https://doi.org/10.1175/JCLI-D-12-00441.1>.
- Wing, A. A., K. Emanuel, and S. Solomon, 2015: On the factors affecting trends and variability in tropical cyclone potential intensity. *Geophys. Res. Lett.*, **42**, 8669–8677, <https://doi.org/10.1002/2015GL066145>.
- Zhang, R., and T. L. Delworth, 2006: Impact of Atlantic multi-decadal oscillations on India/Sahel rainfall and Atlantic hurricanes. *Geophys. Res. Lett.*, **33**, L17712, <https://doi.org/10.1029/2006GL026267>.